Effects of multi-scale heterogeneity on the simulated evolution of ice-rich permafrost lowlands under a warming climate

Jan Nitzbon[1,2,3], Moritz Langer[1,2], Léo C. P. Martin[3], Sebastian Westermann[3], Thomas Schneider von Deimling[1,2], and Julia Boike[1,2]

[1]Permafrost Research, Alfred Wegener Institute Helmholtz Centre for Polar and Marine Research, Potsdam, Germany
[2]Geography Department, Humboldt-Universität zu Berlin, Berlin, Germany
[3]Department of Geosciences, University of Oslo, Oslo, Norway

Correspondence: Jan Nitzbon (jan.nitzbon@awi.de)

Abstract. Thawing of ice-rich permafrost deposits can cause the formation of thermokarst terrain, thereby involving ground subsidence and feedbacks to the thermal and hydrological regimes of the subsurface. Thermokarst activity can entail manifold pathways of landscape evolution and cause rapid permafrost thaw in response to a warming climate. Numerical models that realistically capture these degradation pathways and represent the involved feedback processes at different spatial scales, are

5 required to assess the threats and risks that thermokarst processes pose to the functioning of ecosystems and human infrastructure in the Arctic. In this study, we therefore introduce a multi-scale tiling scheme to the CryoGrid 3 permafrost model which allows to represent the spatial heterogeneities of surface and subsurface conditions, together with lateral fluxes of heat, water, snow, and sediment, at spatial scales not resolved in Earth system models (ESMs). We applied the model setup to a lowland tundra landscape in northeast Siberia characterized by ice-wedge polygons at various degradation stages. We present

10 numerical simulations under a climate-warming scenario and investigate the sensitivity of projected permafrost thaw to different terrain heterogeneities, on both a micro-scale (ice-wedge polygons) and a meso-scale (low-gradient slopes). We found that accounting for both micro- and meso-scale heterogeneities yields the most realistic possibilities for simulating landscape evolution. Simulations that ignored one or the other of these scales of heterogeneity were unable to represent all of the possible spatio-temporal feedbacks in ice-rich terrain. For example, we show that the melting of ice wedges in one part of the

15 landscape can result in the drainage of other parts, where surface water has been impounded a number of decades earlier as a result of ice-wedge thermokarst. We also found that including subgrid-scale heterogeneities in the simulations resulted in a more gradual response in terms of ground subsidence and permafrost thaw, compared to the more abrupt changes in simple one-dimensional simulations. Our results suggest that, under a warming climate, the investigated area is more likely to experience widespread drainage of polygonal wetlands than the formation of new thaw lakes, which is in general agreement with

20 evidence from previous field studies. We also discuss how the presented model framework is able to capture a broad range of processes involved in the cycles of ice-wedge and thaw-lake evolution. The results of this study improve our understanding of how micro- and meso-scale processes control the evolution of ice-rich permafrost landscapes. Furthermore, the methods that we have developed allow improved representation of subgrid-scale processes such as thermokarst in ESMs.

1   Introduction

25   Thawing of permafrost in response to climatic change, poses a threat to ecosystems, infrastructure, and indigenous communities in the Arctic (AMAP, 2017; Vincent et al., 2017; Schuur and Mack, 2018; Hjort et al., 2018). Permafrost degradation involves a wide range of feedback process from local to global scales, including widespread changes in soil moisture (Andresen et al., 2020), and the potential liberation of greenhouse gases, posing a positive feedback to climate warming (Schuur et al., 2015; Schneider von Deimling et al., 2015). However, the large-scale models used to project the response of permafrost

30   to climate warming, employ a simplistic representation of permafrost thaw dynamics, which only reflects gradual top-down thawing of frozen ground (Lawrence et al., 2012; Slater and Lawrence, 2013; Andresen et al., 2020). In particular, such models lack representation of thaw processes in ice-rich permafrost deposits that cause localized and rapid landscape changes called thermokarst (Kokelj and Jorgenson, 2013). Thermokarst activity is induced on small spatial scales that are not resolved in large-scale Earth system models (ESMs), but it can have widespread effects on the ground thermal and hydrological regimes

35   (Fortier et al., 2007; Liljedahl et al., 2016), soil erosion (Godin et al., 2014), and on carbon decomposition pathways (Lara et al., 2015; Turetsky et al., 2020). In addition, thermokarst features can induce positive feedback processes leading to accelerated permafrost degradation and landscape collapse (Walter Anthony et al., 2018; Turetsky et al., 2019; Farquharson et al., 2019; Nitzbon et al., 2020), but also stabilizing feedbacks have been observed (Jorgenson et al., 2015; Kanevskiy et al., 2017), overall establishing thermokarst as a key factor of uncertainty in any future projections of how permafrost and hydrology respond to

40   Arctic climate change.

To address these issues, numerical models resolving heterogeneities at the spatial scales of thermokarst features and representing the vertical and lateral physical processes that give rise to the complex pathways of permafrost landscape evolution observed in the real world are required (Rowland et al., 2010). In recent years, substantial progress has been made in the development of numerical models to study the thermal and hydrological dynamics of permafrost terrain on small scales (Painter

45   et al., 2016; Jafarov et al., 2018), and to identify important feedbacks associated with various thermokarst landforms such as ice-wedge polygons (Abolt et al., 2018; Nitzbon et al., 2019; Abolt et al., 2020) or peat plateaus (Martin et al., 2019). The development of numerical schemes simulating ground subsidence resulting from excess ice melt (Lee et al., 2014; Westermann et al., 2016) enabled the assessment of transient changes of thermokarst terrain using dedicated permafrost models (Langer et al., 2016; Nitzbon et al., 2019), but also more broadly using ESM framworks (Aas et al., 2019).

50   Using a tile-based modelling approach to represent lowlands underlain by massive ice wedges, Nitzbon et al. (2020) recently suggested the potential for substantial permafrost degradation in northeast Siberia in response to a warming climate, which is not captured by large-scale models that ignore thermokarst-inducing processes. These projections revealed a considerable uncertainty range associated with different hydrological boundary conditions in the simulations, that gave rise to contrasting pathways of landscape evolution, ranging from the development of high-centred polygons (HCPs) to the formation of thaw

55   lakes. This uncertainty can be attributed to the fact that while the numerical model explicitly incorporates the micro-scale heterogeneity of ice-wedge polygon terrain (i.e., meters to tens of meters), it did not explicitly reflect meso-scale (i.e., hundreds to thousands of meters) landscape dynamics (see Table 1 for the terminology used to refer to different spatial scales). For

example, kilometer-scale mapping of ice-wedge polygon types at different Arctic sites revealed, that polygons of the same degradational stage are located close to each other, but that there is a variability of different polygon types at the meso-scale

60 (Kartoziia, 2019; Abolt and Young, 2020). These patterns could thus be linked to lateral surface and subsurface water fluxes which follow the terrain's topography and affect the degradation of ice wedges (Nitzbon et al., 2019). Moreover, excess ice melt on the micro-scale, can lead to the emergence of thaw features and feedbacks on the meso-scale, such as the formation of drainage networks (Liljedahl et al., 2016), laterally expanding thaw lakes, or thermo-erosional gullies. These features have the potential to interact with each other, thereby adding more complexity to the landscape evolution, for example, when a thaw

65 lake drains upon incision of the thermo-erosional gully. Hence, in order to constrain the most likely landscape evolution and permafrost degradation pathways further, landscape heterogeneity and lateral processes at the meso-scale need to be considered. Tiling schemes which proved successful in realistically reflecting micro-scale permafrost dynamics (Aas et al., 2019), constitute a promising approach to also capture meso-scale processes in order to constrain those uncertainties further while keeping computational costs low.

70   In this study, we employ a multi-scale hierarchical tiling approach to investigate the transient response of ice-rich permafrost lowlands in northeast Siberia to projected twenty-first century climate warming. Specifically, we address the following objectives:

1. To investigate the transient evolution of ice-rich permafrost landscapes in response to climate warming using different representations of micro- and meso-scale heterogeneity, thereby identifying degradation pathways and feedback pro-

75   cesses associated with lateral fluxes on these different spatial scales.

2. To quantify the sensitivity of projected permafrost thaw and ground subsidence to different representations of micro- and meso-scale heterogeneity.

Overall, our study intends to provide a transferable and scalable framework for more robustly assessing ice-rich permafrost landscape evolution, and at the same time aims at reducing sources of uncertainty in the projections of ice-rich permafrost

80 response to a warming climate presented by Nitzbon et al. (2020). Instead of providing quantitative site-specific projections, the presented simulations should thus be considered as numerical experiments to explore important scales and controls of ice-rich permafrost landscape dynamics in response to a warming climate.

2 Methods

2.1 Terminology for spatial scales

85   Throughout the manuscript we use a consistent terminology to refer to different characteristic length scales of landscape features and processes. This terminology is summarized in Table 1.

Terminology	Superscript	Length scale	Example
subgrid	–	$\lesssim 10^5 \, \mathrm{m}$	all mentioned below
micro	μ	$\simeq 10^0 - 10^1 \, \mathrm{m}$	Ice-wedge polygon micro-topography
meso	m	$\simeq 10^2 - 10^3 \, \mathrm{m}$	Thermo-erosion catchments, thaw lakes
macro	–	$\simeq 10^4 - 10^5 \, \mathrm{m}$	River delta, ESM grid cell

Table 1. Overview of the terminology used in this manuscript to refer to the spatial scale of permafrost landscape features and processes.

2.2 Study area

While the the scientific objectives and the modelling concept pursued in this study are general and applicable to any ice-rich continuous permafrost terrain, we chose Samoylov Island in the Lena river delta in northeast Siberia as our focus study
90   area ($72.36972\,°$N, $126.47500\,°$E). The island is located in the central southern part of the Lena River delta within the lowland tundra vegetation zone and features cold continuous permafrost (mean annual ground temperature of about $-9\,°$C (Boike et al., 2019)), which has been warming rapidly in recent years (about $0.9\,°$C per decade (Biskaborn et al., 2019)).

Samoylov Island belongs to the first terrace of the Lena River delta which formed during the Holocene (Schwamborn et al., 2002). The fluvial deposits contain substantial amounts of excess ice, mainly in form of ice wedges up to $10\,\mathrm{m}$ deep, which
95   can be of epigenetic and syngenetic type. The surface of the island is characterized by ice-wedge polygons and water bodies of different sizes, ranging from ponds in polygon troughs and centers to thermokarst lakes several hundred meters in diameter (Figure 1 a). While the low-lying western part of Samoylov Island is regularly flooded in spring, the eastern part is more elevated but with an overall very flat topography (Fig. 1 a). Ice-wedge polygons show different features across different parts of the island, including mostly low-centered polygons with water-covered centers, but also water-filled troughs indicative of
100   ice-wedge degradation, and some high-centered polygons with drained troughs. Polygons of different geomorphological type tend to occur as grouped "clusters" in the same areas of the island (Kartoziia, 2019), and the pre-dominant types differ along gently-sloped (about 0.1%) transects across the island (Fig. 1 b).

Meteorological and ground conditions have been measured on Samoylov Island for almost two decades, establishing it as a key site for the long-term monitoring of permafrost and the validation of numerical models (Boike et al., 2013, 2019).
105   Various field studies addressed the climatology, hydrology, and geomorphology of the Island on different scales (Boike et al., 2008; Langer et al., 2011a, b; Muster et al., 2012), allowing the calibration and evaluation of numerical models used to assess
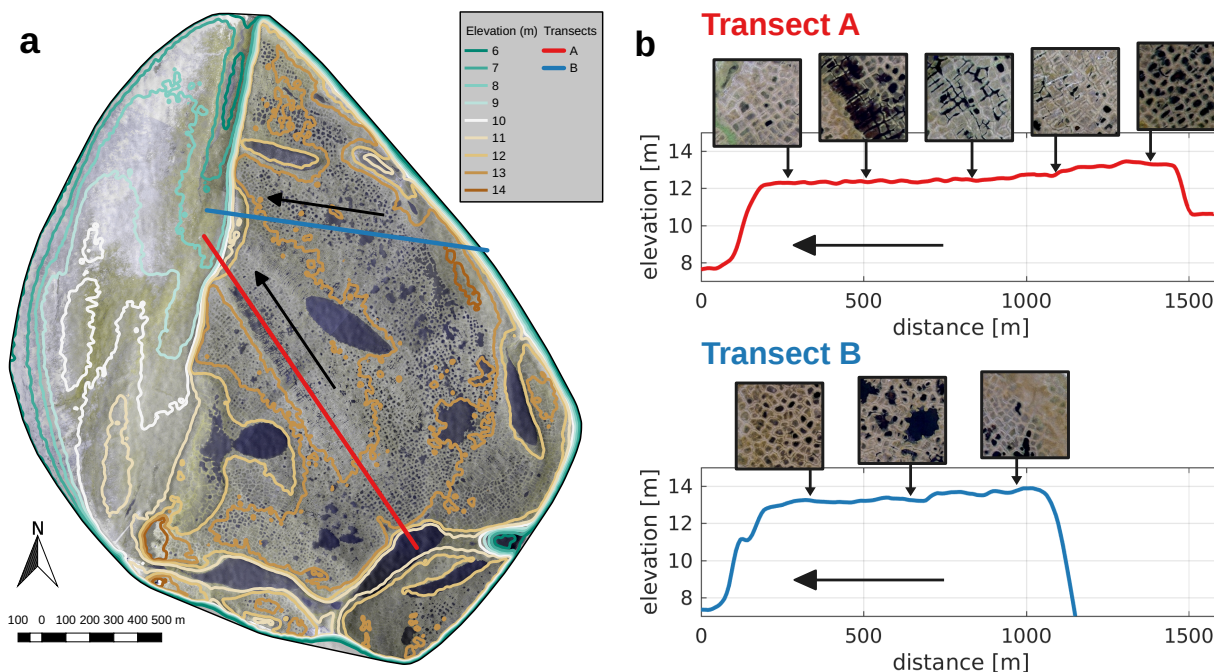
Figure 1. a: Aerial photography of Samoylov Island with elevation contour lines based on the ArcticDEM. The study area is covered with water bodies of different sizes and ice-wedge polygons of different geomorphological stages. b: Two (arbitrary) examples of transects across the island, reflecting the gently-sloped terrain with steep cliffs at the margins. The inlets are details (about $100\,\mathrm{m}$ in diameter) of the aerial photography, reflecting polygon clusters of similar stages along the transects. Arrows point towards the main drainage direction. Note that ice-wedge polygons show little signs of degradation in the highest-elevated parts and close to the margins of the island (first and last inlet of both Transects). Along Transect A, the abundance of thermokarst troughs increases in the downstream direction of the slope. Small water bodies are visible in the central part of Transect B.

permafrost dynamics in northeast Siberia under recent (Gouttevin et al., 2018; Nitzbon et al., 2019) and future (Westermann et al., 2016; Langer et al., 2016; Nitzbon et al., 2020) climatic conditions.

2.3 Model description

2.3.1 Process representations (CryoGrid 3 Xice)

For the numerical experiments in this study, we used the CryoGrid 3 (Xice) permafrost model, which is a physical process-based land surface model tailored for applications in permafrost environments (Westermann et al., 2016). CryoGrid 3 has a one-dimensional representation of the subsurface for which it computes the subsurface temperatures ($T(z,t)$ [$°C$]) by solving the heat diffusion equation, thereby taking into account the phase change of soil water (θ_{w} [-]) through an effective heat

capacity:

$$\left(C(z,T) + \rho_w L_{sl} \frac{\partial \theta_w}{\partial T}\right) \frac{\partial T}{\partial t} = \frac{\partial}{\partial z}\left(k(z,T)\frac{\partial T}{\partial z}\right) . \qquad (1)$$

In Equation (1), $C(z,T)$ is the volumetric heat capacity of the soil, $k(z,T)$ the thermal conductivity of the soil, both parameterized depending on the soil constituents. ρ_w [kg m^{-3}] is the density of water, and L_{sl} [J kg^{-1} K^{-1}] the specific latent heat of fusion of water. The upper boundary condition to Eq. (1) is prescribed as a ground heat flux which is obtained by solving the surface energy balance (Westermann et al., 2016). CryoGrid 3 simulates the dynamic build-up and ablation of a snow pack above the surface, heat conduction through the snowpack, changes to the snowpack due to infiltration and refreezing of rain and meltwater, and changes in snow albedo due to aging (Westermann et al., 2016). Snow is deposited at a constant density ($\rho_{snow} = 250$ kg m^{-3}) which can effectively increase due to infiltration and refreezing of water. The model further employs a simple vertical hydrology scheme to represent changes in the ground hydrological regime due to infiltration of rain or meltwater, and evapotranspiration (Martin et al., 2019; Nitzbon et al., 2019). Excess water is allowed to pond above the surface, and heat transfer through unfrozen surface water bodies is represented assuming complete mixing of the water column throughout the ice-free period (Westermann et al., 2016). The field capacity parameter was set to $\theta_{fc} = 0.5$.

CryoGrid 3 represents a range of physical processes which enable it to simulate the formation of thermokarst in ice-rich permafrost deposits Westermann et al. (2016); Langer et al. (2016); Nitzbon et al. (2019, 2020). Soil layers which have an ice content (θ_i) exceeding the natural porosity (ϕ_{nat}) of the soil constituents, are treated as excess ice layers. Once an excess ice layer thaws, the resulting excess water $\theta_i - \phi_{nat}$ is routed upwards, while above-lying soil constituents are routed downwards, following the scheme proposed by Lee et al. (2014). Thawing of an excess ice layer of thickness Δp thus results in a net subsidence (Δs) of the ground surface:

$$\Delta s = \Delta p \underbrace{\frac{\theta_i - \phi_{nat}}{1 - \phi_{nat}}}_{\theta_x} , \qquad (2)$$

where θ_x denotes the excess ice content of the ice-rich soil layer.

The thermal regime and thaw processes in ice-rich permafrost are further controlled by lateral fluxes of mass and energy at subgrid-scales. We used the concept of laterally coupled tiles (Langer et al., 2016; Nitzbon et al., 2019) to represent subgrid heterogeneity of permafrost terrain (see Section 2.3.2 for details). We followed Nitzbon et al. (2019) to represent lateral fluxes of heat, water, and snow between adjacent tiles at the micro-scale. Furthermore, we included micro-scale advective sediment transport due to slumping, following the scheme introduced by Nitzbon et al. (2020). For this study, we advanced the model capacities by taking into account lateral fluxes of water on the meso-scale, for which we further distinguished between surface fluxes and subsurface contributions. Both surface and subsurface fluxes were calculated according to a gradient in water table elevations following Darcy's law, but the hydraulic conductivities differed considerably ($K^{subs} = 10^{-5}$ m s^{-1}, $K^{surf} = 10^{-2}$ m s^{-1}; see Appendix A for details). Finally, our model allowed for lateral drainage of water, by assuming an external reservoir at a fixed elevation (e_{res}) and a constant effective hydraulic conductivity ($K_{res} = 2\pi K_{subs}$) as hydrological boundary condition for a tile.

2.3.2 Multi-scale hierarchical tiling

For the present study, we extended the concept of laterally coupled tiles (Langer et al., 2016; Nitzbon et al., 2019) to a multi-scale hierarchical approach that allows to represent the subgrid-scale heterogeneity of permafrost terrain in general, and of thermokarst processes in particular. The multi-scale tiling hierarchy can flexibly be adapted to represent heterogeneous permafrost landscapes and features across several spatial scales. Different numbers of micro-scale tiles (N^μ) and meso-scale tiles (N^m) are used to reflect heterogeneity at different subgrid-scales. Each of the tiles is associated with a one-dimensional representation of the subsurface.

While the concept of the multi-scale tiling is very general, we applied it for the present study to create the subsequent four model setups (see Figure 2):

- *Homogeneous* ($N^\mu = 1$, $N^\mathrm{m} = 1$, Figure 2 a): This is the most simple case which reflects homogeneous surface and subsurface conditions across all spatial scales via only one tile (H). Water can drain laterally into an external reservoir at a fixed elevation (e_res). This setup comes closest to the simplistic representation of permafrost in ESMs and corresponds to the set-up for the simulations presented in Westermann et al. (2016).

- *Polygon* ($N^\mu = 3$, $N^\mathrm{m} = 1$, Figure 2 b): This setting reflects the micro-scale heterogeneity associated with ice-wedge polygons via three tiles: polygon centers (C), polygon rims (R) and inter-polygonal troughs (T). The heterogeneity of the surface topography is expressed in different initial elevations of the soil surface of the tiles. The subsurface stratigraphies of the tiles differ with respect to the depth (d_x) and amount (θ_x) of excess ice, reflecting the network of ice wedges linked to the polygonal surface pattern. Lateral fluxes of heat, water, snow, and sediment is enabled among the tiles, and the trough tile is connected to an external water reservoir. This configuration has been used by Nitzbon et al. (2019) and Nitzbon et al. (2020). The characteristics of the polygon setting are summarized in Table 3.

- *Homogeneous landscape* ($N^\mu = 1$, $N^\mathrm{m} = 3$, Figure 2 c): This setup reflects a meso-scale gradient of slope S^m, for which the outer tile (H$^\mathrm{o}$) is connected to a low-lying reservoir (well-drained). The intermediate (H$^\mathrm{m}$) and inner (H$^\mathrm{i}$) tiles represent the landscape upslope of the well-drained tile (drainage point) at constant distances (D^m). The setting assumes a translational symmetry perpendicular to the direction of the slope, i.e. each tile represents an equal total area at the meso-scale. Lateral surface and subsurface water fluxes are enabled among the meso-scale tiles, while lateral heat fluxes as treated by Langer et al. (2016) were not considered in this study.

- *Polygon landscape* ($N^\mu = 3$, $N^\mathrm{m} = 3$, Figure 2 d): This setup reflects a meso-scale slope featuring ice-wedge polygons at the micro-scale. Each meso-scale tile is represented by three tiles (C,R,T) at the micro-scale, corresponding to the *polygon* setup described above. However, only the trough tile of the outer polygon (T$^\mathrm{o}$) is connected to a low-lying reservoir (well-drained), and the intermediate and inner troughs are hydrologically connected along the meso-scale slope.
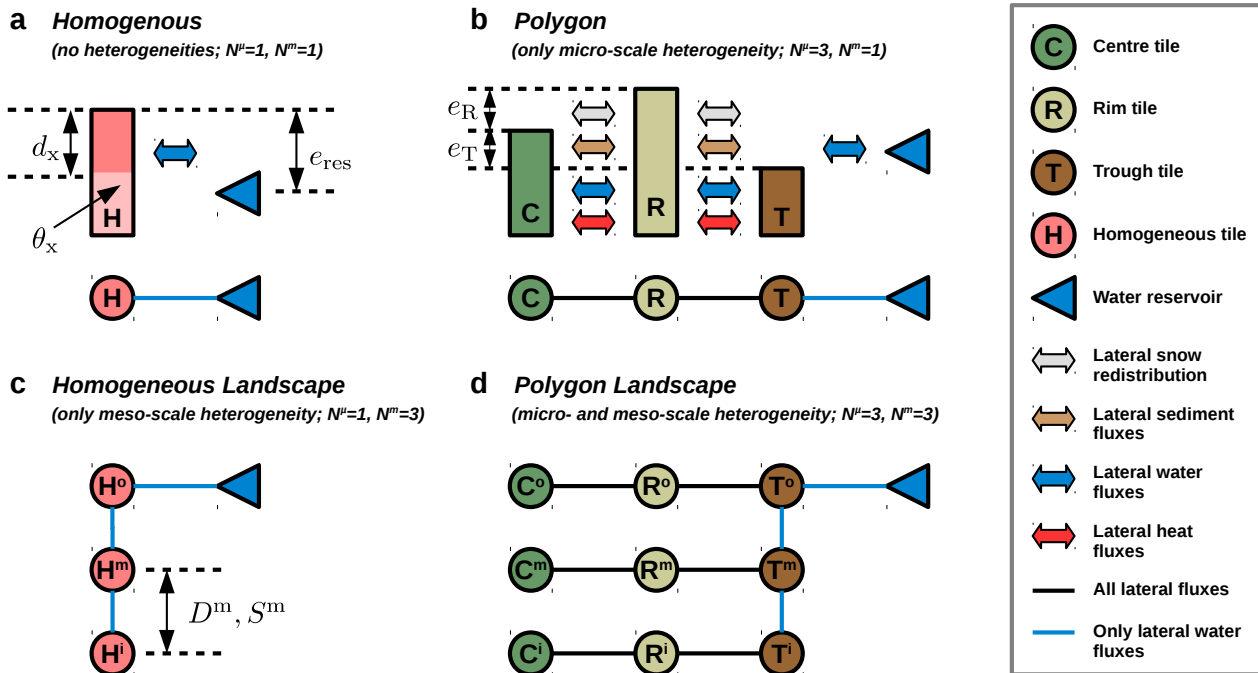
7

Figure 2. Overview of the the different tile-based model setups used to represent heterogeneity at micro- and meso-scales. The depth of excess ice (d_x) and the excess ice content (θ_x) determine the distribution of excess ground ice in each of the tiles. An external reservoir (blue triangle) at a fixed elevation (e_{res}) prescribes the hydrological boundary conditions. Note that d_x and θ_x for the simple tile are chosen such that they correspond to the area-weighted mean of the three tiles of the polygon setup.

a: The *homogeneous* setup used only one tile (H) and does not reflect any subgrid-scale heterogeneity.

b: The *polygon* setup reflects micro-scale heterogeneity of topography and ground ice distribution associated with ice-wedge polygons via three tiles: polygon centres (C), polygon rims (R) and inter-polygonal troughs (T). The parameters e_R and e_T indicate the (initial) elevation of rims and troughs relative to the center. The micro-scale tiles are interacting through lateral fluxes of heat, water, snow, and sediment.

c: The *homogeneous landscape* setup reflects meso-scale heterogeneity of an ice-rich lowland via three tiles ($H^{o,m,i}$) of which the outer one (H^o) is connected to a draining reservoir. The intermediate (H^m) and inner tiles (H^i) are located at distances D^m along a low-gradient slope S^m. The meso-scale tiles are interacting through lateral surface and subsurface water fluxes.

d: The *polygon landscape* setup incorporates heterogeneities at both micro- and meso-scales via a total of nine tiles.

2.4 Model settings and simulations

2.4.1 Soil stratigraphies and ground ice distribution

The subsurface of all tiles is represented via a generic soil stratigraphy (Table 2). The stratigraphy is based on previous studies
180 using CryoGrid 3 for the same study area (Nitzbon et al., 2019, 2020). It consists of two highly porous layers of $0.1\,\mathrm{m}$ thickness

which reflect the surface vegetation and an organic-rich peat layer. Below that a mineral layer with silty texture follows. An excess ice layer of variable ice content θ_i extends from a variable depth d_x down to a depth of $10.0\,\mathrm{m}$. Between the variable excess ice layer and the mineral layer, an ice-rich intermediate layer of $0.2\,\mathrm{m}$ thickness is placed. Below the variable excess ice layer follow an ice-poor layer and bedrock down to the end of the model domain.

185   The default ice content assumed for the excess ice layer of homogeneous tiles (no micro-scale heterogeneity) was $\theta_i^{\mathrm{H}} = 0.75$ and the default depth of this layer was $d_x = 0.9\,\mathrm{m}$. To reflect the heterogeneous excess ice distribution associated with ice-wedge polygons, different ice contents were assumed for the excess ice layers of polygon centres ($\theta_i^{\mathrm{C}} = 0.65$), rims ($\theta_i^{\mathrm{R}} = 0.75$), and troughs ($\theta_i^{\mathrm{T}} = 0.95$). However, the area-weighted mean excess ice content of ice-wedge polygon terrain is identical to the default value assumed for simple tiles (Table 3).

Table 2. Generic soil stratigraphy used to represent the subsurface of all tiles. An ice-rich layer of variable ice content (θ_i) is located at variable depth (d_x) from the surface. Note that the effective excess ice content (θ_x) is linked to the absolute ice content (θ_i) and the natural porosity (ϕ_{nat}) via the relation given in Equation (2). The soil texture is only used to parameterize the freezing-characteristic curve of the respective layer.

Depth from [m]	Depth to [m]	Mineral θ_{m}	Organic θ_{o}	Nat. por. ϕ_{nat}	Soil texture	Water θ_{w}^0	Comment
0	0.1	0	0.15	0.85	sand	0.85	Vegetation layer
0.1	0.2	0.10	0.15	0.75	sand	0.75	Organic layer
0.2	$d_x - 0.2$	0.25	0.10	0.65	silt	0.65	Mineral layer
$d_x - 0.2$	d_x	0.20	0.15	0.55	sand	0.65	Intermediate layer
d_x	10	$\frac{1.05-\theta_i}{2}$	$\frac{0.95-\theta_i}{2}$	0.55	sand	θ_i	Variable excess ice layer
10	30	0.50	0.05	0.45	sand	0.45	Ice-poor layer (Taberit)
30	1000	0.90	0	0.10	sand	0.10	Bedrock

2.4.2 Topography

190

For the *homogeneous* setup (Figure 2 a) the initial altitude of the soil surface was assumed to be $20.0\,\mathrm{m}$ above sea level, corresponding roughly to the altitude of the study area (see Section 2.2). This value does not affect the simulation results, but it serves as a reference for the variation of the micro- and meso-scale topographies. For the *polygon* setup (Figure 2 b) we assumed that the rims were elevated by $e_{\mathrm{R}} = 0.2\,\mathrm{m}$ relative to the polygon centres, while the troughs had the same altitude as the centres ($e_{\mathrm{T}} = 0.0\,\mathrm{m}$). While this choice of parameters varies slightly from the values assumed in previous studies (Nitzbon et al., 2019, 2020), it allows for consistent comparability to the setups without micro-scale heterogeneity (Table 3).

195

    The meso-scale topography in the *homogeneous landscape* setup (Figure 2 c) was obtained by multiplying the meso-scale distances (D^{m}) with the slope of the terrain (S^{m}). We set $D^{\mathrm{m}} = 100\,\mathrm{m}$ and $S^{\mathrm{m}} = 0.001$ for all *landscape* setups, yielding elevations of $0.1\,\mathrm{m}$ and $0.2\,\mathrm{m}$ relative to the outer tile for the intermediate and inner tiles, respectively. The micro-scale topography of the *polygon landscape* setup (Figure 2 d) was obtained by adding up the relative topographic elevations of the meso- and micro-scales.

200

2.4.3 Topology

We made simplifying assumptions to determine the adjacency and geometrical relations such as distances and contact lengths between the tiles at the micro- and meso-scale. These topological characteristics determine the magnitude of lateral fluxes

205 between the tiles, and only need to be specified if more than one tile is used to represent the respective scale. For the polygon setup at the micro-scale we assumed a geometry of a circle (C) surrounded by rings (R,T), following Nitzbon et al. (2020). This geometry is fully defined by specifying the total area (A^μ) of a single polygonal structure and the areal fractions ($\gamma_{\mathrm{C,R,T}}$) of the three tiles. Here we chose values which constitute a compromise between observations from the study area and comparability to the setups without micro-scale heterogeneity (Table 3). For this geometry, the micro-scale distances D^μ and contact lengths

210 L^μ can be calculated as provided in the Supplementary Information to Nitzbon et al. (2020).

For the *landscape* setups with three meso-scale tiles we assumed translational symmetry of the landscape in the direction perpendicular to the direction of the gradient. Furthermore, the three meso-scale tiles were assumed to be at equal distances of $D^{\mathrm{m}} = 100\,\mathrm{m}$ from each other. Hence, each meso-scale tile is representative for the same areal fraction of the overall landscape. For the translational symmetry, it is sufficient to specify D^{m} in order to calculate the lateral surface and subsurface water fluxes.

Parameter	Symbol	Unit	Tile				
			C	R	T	∅ / Σ	H
Stratigraphy							
Depth of excess ice layer	d_{x}	[m]	1.0	0.9	0.7	0.9	0.9
Ice content of excess ice layer	θ_{i}	[-]	0.65	0.75	0.95	0.75	0.75
Topography and Topology							
Areal fraction	γ	[-]	$\frac{1}{3}$	$\frac{1}{2}$	$\frac{1}{6}$	1	1
Total area	A^μ	[m^2]	–	–	–	140	1
Initial elevation	e	[m]	0.0	0.2	0.0	0.1	0.0
Hydrological boundary conditions							
Reservoir elevation poorly-drained	$e_{\mathrm{res}}^{\mathrm{pd}}$	[m]	–	–	0.0	0.0	−0.1
Reservoir elevation well-drained	$e_{\mathrm{res}}^{\mathrm{wd}}$	[m]	–	–	−10.0	−10.0	−10.0

Table 3. Overview of the model parameters for different representations of the micro-scale. Elevation values are given relative to the initial altitude of the center tile ($a_{\mathrm{C}} = 20.0\,\mathrm{m}$). Note that on average the *polygon* setup (C,R,T) exhibits the same characteristics as the *homogeneous* setup (H). Note that setting the area of the simple tile to $A^\mu = 1\,\mathrm{m}^2$ is an arbitrary choice, as it cancels out during the calculation of the meso-scale fluxes due to the assumed symmetry.

215 2.4.4 Forcing data

We used the same meteorological forcing dataset which has been used in preceding studies based on CryoGrid 3 for the same study area (Westermann et al., 2016; Langer et al., 2016; Nitzbon et al., 2020). The dataset spans the period from 1901 until 2100 and is based on down-scaled CRU-NCEP v5.3 data for the period until 2014. For the period after 2014 climatic anomalies

obtained from CCSM4 projections for the RCP8.5 scenarios were applied to a repeatedly appended base climatological period.

220   A detailed description of how the forcing dataset was generated is provided by Westermann et al. (2016).

2.4.5   Simulations

To investigate the sensitivity to the micro-scale representation and to compare the *landscape* setup to the setups without meso-scale heterogeneity we conducted a total of six simulations. For each micro-scale representation (*homogeneous* versus *polygon*) we conducted three simulations under the RCP8.5 warming scenario: *well-drained*, *poorly-drained*, *landscape*.

225   The well-drained and poorly-drained cases for the *polygon* setup correspond to the confining cases considered in Nitzbon et al. (2020), and reflect contrasting hydrological boundary conditions (Table 3). For the well-drained case, the elevation of external reservoir was set to $e_{res}^{wd} = -10.0\,\mathrm{m}$, independent of the micro-scale representation. For the poorly-drained case, the elevation of the external reservoir was set to $e_{res}^{pd} = -0.1\,\mathrm{m}$ (*homogeneous*) and $e_{res}^{pd} = 0.0\,\mathrm{m}$ (*polygon*), respectively. For the *landscape* simulations, only one tile (H° and T°, respectively) was connected to an external reservoir (Fig. 2 c,d; $e_{res}^{wd} = -10.0\,\mathrm{m}$), while

230   the hydrological boundary fluxes of the intermediate and inner tiles resulted from adjacent tiles only.

The subsurface temperatures of each model run were initialized in 10/1999 with a typical temperature profile for that time of year which was based on long-term borehole measurements from the study area (Boike et al., 2019). Using multi-year spin-up periods did not result in significant changes to the near-surface processes investigated in this study so that uncertainty related to the initial condition can be excluded. The analyzed simulation period was the twenty-first century from 01/2000 until 12/2099.

3 Results

3.1 Landscape evolution

3.1.1 Simulations without micro-scale heterogeneity

The simulated landscape evolution for selected years throughout the twenty-first century under RCP8.5 for all runs with a homogeneous micro-scale representation (setups presented in Fig. 2 a,c) is visualized in Figure 3.

Single-tile simulations: Until 2050 no excess ice melt and associated ground subsidence occur in both the well-drained and the poorly-drained single-tile simulations (Fig. 3 a–c, first and fifth column). Between 2050 and 2075 excess ice melt occurs in both single-tile simulations and leads to ground subsidence by about $0.2\,\text{m}$ in the well-drained case, and by about $0.5\,\text{m}$ in the poorly-drained case (Fig. 3 d, first and fifth column). In the poorly-drained simulation excess ice melt leads to the formation of a shallow surface water body. By 2100 total ground subsidence reaches almost $1.0\,\text{m}$ in the well-drained simulation (Fig. 4 e, first column). In the poorly-drained simulation, excess ice melt proceeds faster than in the well-drained case, causing the surface water body to deepen, and to reach a depth of about $2.0\,\text{m}$ by 2100 (Fig.3 e, fifth column). A talik of about about $1.5\,\text{m}$ thickness has formed in this simulation by the end of the simulation period.

Landscape simulations: The simulated evolution of the outer tile in the landscape simulation is very similar to that of the well-drained single-tile throughout the simulation period (Fig. 3 first and second column). In the intermediate and inner tiles of the landscape simulation, melting of excess ice and associated ground subsidence occur during the first half of the simulation period, and there is a shallow layer of surface water (about $0.2\,\text{m}$) in these tiles (Fig. 3 a–c, third and fourth column). After 2050 excess ice melt proceeds faster and the surface water body in the intermediate and inner tiles reaches a depth of almost $1\,\text{m}$ by 2075 (Fig. 3 d, third and fourth column). The permafrost table in these tiles lowered by about $2\,\text{m}$ relative to its initial position. Between 2075 and 2100 a talik of about $2\,\text{m}$ thickness forms beneath the water body in the two inland tiles (Fig. 3 e, third and fourth column). By 2100 the water body has a depth of about $1.5\,\text{m}$ in both tiles.

The ground subsidence in the outer tile during the second half of the simulation leads to a lowering of the water level of the surface water body in the intermediate and inner tiles (Fig. 3 d–e). As a result, the surface water body depth by 2100 is about $1.5\,\text{m}$ in the landscape simulation, while it is about $2.0\,\text{m}$ in the poorly-drained single-tile simulation (Fig. 3 e, third to fifth column). This difference in water body depths is observed despite excess ice melt and surface water formation in the landscape simulation set on several decades earlier than in the poorly-drained single-tile simulation.
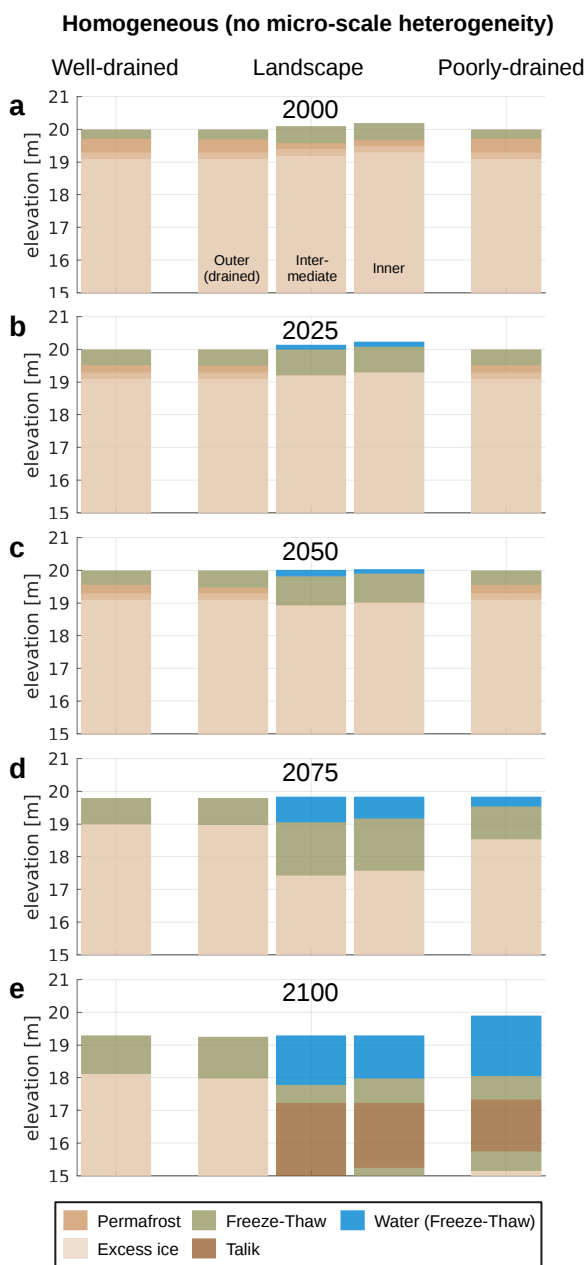
Figure 3. Landscape evolution in the simulations with a homogeneous micro-scale representation under the RCP8.5 warming scenario. The well-drained and poorly-drained cases correspond to the model setup without micro- or meso-scale heterogeneity (Fig. 2 a) and the landscape case corresponds to the model setup with only meso-scale heterogeneity (Fig. 2 c).

3.1.2 Simulations with micro-scale heterogeneity reflecting ice-wedge polygons

In analogy to Figure 3, Figure 4 illustrates the landscape evolution throughout the twenty-first century under RCP8.5 for the simulations with the micro-scale heterogeneity reflecting ice-wedge polygons. In addition, it shows the geomorphological state of the polygon micro-topography, i.e., whether it is low-centered (LCP), intermediate-centered (ICP), or high-centered (HCP), or turned into a water body (WB), according to the definitions in Nitzbon et al. (2020). Initially, all simulations feature undegraded ice-wedge polygons with an LCP micro-topography (Fig. 4 a).

Single-polygon simulations: Between 2000 and 2050, initial ice-wedge degradation occurs in the well-drained single-polygon simulation, indicated by subsiding troughs and a transition from the LCP to the ICP micro-topography (Fig. 4 a–c, first column). Between 2050 and 2075, substantial excess ice melt occurs in the trough and rim tile, leading to a transition to a pronounced HCP micro-topography for the well-drained polygons (Fig. 4 d, first column). The degradation continues until 2100, when the trough tile has subsided by about $2\,\mathrm{m}$, the rim tile by about $1\,\mathrm{m}$, and the center tile by more than $0.2\,\mathrm{m}$. As a consequence of the connection to a low-lying external reservoir (see Table 3) the well-drained polygon does not show any surface water formation throughout the simulation period.

In contrast, a shallow surface water body of about $0.5\,\mathrm{m}$ depth forms between 2000 and 2025 in the poorly-drained single-polygon simulation, as a result of excess ice melt in the center, rim, and trough tiles (Fig. 4 b, fifth column). The bottom of the water body has a high-centered topography. Little excess ice melt occurs in this polygon between 2025 and 2050 (Fig. 4 c, fifth column). After 2050 excess ice melt proceeds faster, causing the water body to deepen, reaching a depth between $1\,\mathrm{m}$ (center tile) and more than $2\,\mathrm{m}$ (trough tile) by 2075 (Fig. 4 d, fifth column). Until 2100 excess ice melt proceeds further, resulting in a water body depth of $2-4\,\mathrm{m}$ and the formation of an extended talik underneath (Fig. 4 e, fifth column). By the end of the simulation period, the lake is not entirely bottom-freezing in winter.

Polygon landscape simulation: The outer polygon in the landscape simulation shows a very similar evolution to the well-drained single-polygon throughout the entire simulation period (Fig. 4, first and second column). The intermediate and inner polygons show an evolution which is similar to each other, but different from both single-polygon simulations (Fig. 4, third and fourth column). Between 2000 and 2025 excess ice melt in the rim and trough tiles cause the ponding of surface water in the intermediate and inner polygons (Fig. 4 b, third and fourth column) with the surface of the center being close to or elevated above the water table. Besides a lowering of the water table, the configuration of these high-centered polygons does not change much until 2050 (Fig. 4 c, third and fourth column). Between 2050 and 2075, excess ice melt continues, leading to a pronounced high-centered topography (Fig. 4 d, third and fourth column). Meanwhile, the surface water disappears from the rim and trough tiles, as a consequence of marked ice-wedge degradation in the outer polygon (Fig. 4 d, second column). The elevation in the trough tiles increases toward the inland tiles, allowing an efficient drainage of the entire landscape. After 2075 all polygons of the landscape simulation show a similar evolution, resulting in pronounced high-centered topographies with troughs about $2\,\mathrm{m}$ deep and rims that subsided by about $1\,\mathrm{m}$ by 2100. Note that between 2075 and 2100 the troughs of the intermediate and inner polygons subsided more than that of the outer polygon, so that the drainage efficiency is decreased and surface water starts to pond again in the intermediate and inner troughs (Fig. 4 e, third and fourth column).
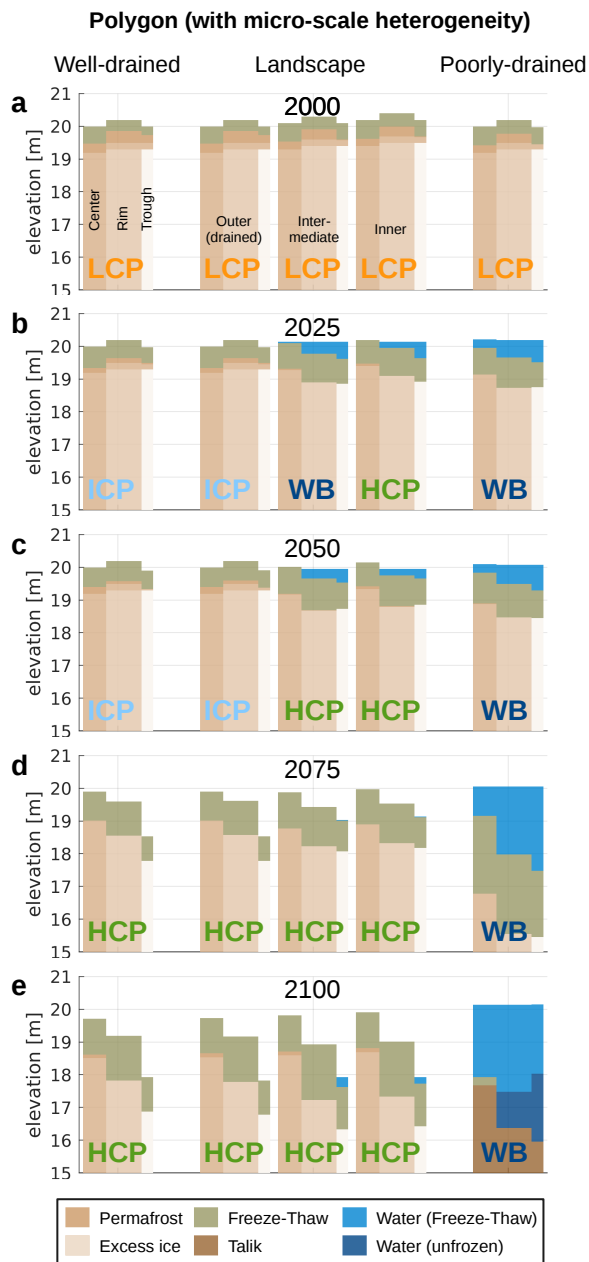
Figure 4. Landscape evolution in the simulations with a polygon micro-scale representation under the RCP8.5 warming scenario. The well-drained and poorly-drained cases correspond to the model setup with only micro-scale heterogeneity (Fig. 2 b) and the landscape case corresponds to the model setup with both micro- and meso-scale heterogeneity (Fig. 2 d). Note that the horizontal width of the tiles does not match with the vertical scale. Based on the relative soil surface elevations of the polygons, these were classified in to low-centered (LCP), intermediate-centered (ICP), high-centered (HCP), and water body (WB), following the definitions in Nitzbon et al. (2020). The same legend as in Fig. 3 applies.

3.2 Permafrost thaw and ground subsidence

295

The changes in the landscape configuration described in the previous section are linked to the degradation of ice-rich rich permafrost, which causes ground subsidence and alters lateral hydrological fluxes in the multi-tile settings. The projected quantitative changes in terms of maximum thawed ground depth and accumulated ground subsidence are displayed in more detail in Figure 5. Note that the sum of thaw-depth increase (i.e., active-layer-deepening) and accumulated ground subsidence

300   correspond to the absolute lowering of the permafrost table.
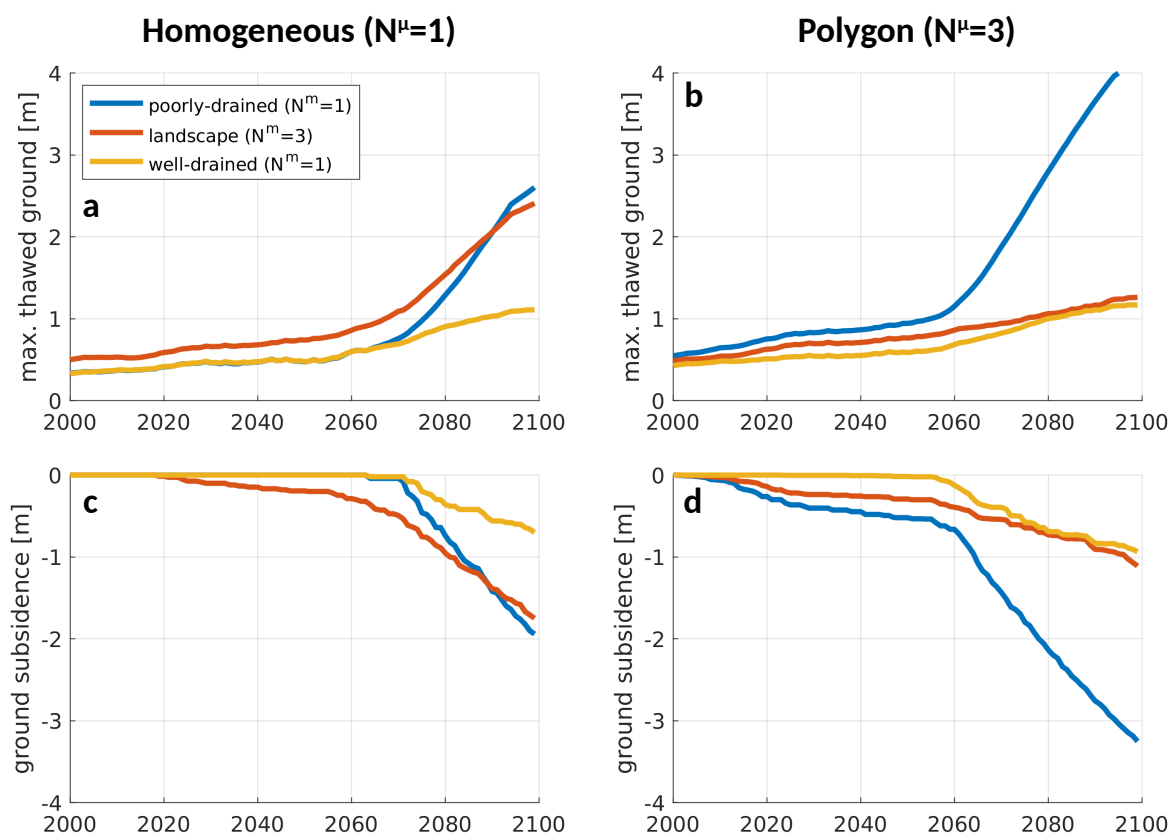
Figure 5. 11-year running mean of maximum annual thawed ground extent (a,b) and the accumulated ground subsidence (c,d) for different micro-scale representations (homogeneous and polygon).

3.2.1 Simulations without micro-scale heterogeneity

Maximum thawed ground: In all simulations without micro-scale heterogeneity, the maximum thawed ground extent increases steadily from less than $0.5\,\mathrm{m}$ in the year 2000 until it roughly has doubled around the years 2070 (Fig. 5 a). Throughout this period, thawed ground is slightly higher in the landscape simulation than in the single-tile simulations. The thawed ground

305   extents in the single-tile simulations diverge during the last three decades of the simulation, with the increase being about two
to three times faster in the poorly-drained (about $2.6\,\mathrm{m}$ in 2100) than in the well-drained simulation (about $1.1\,\mathrm{m}$ in 2100).
Thawed ground extent in the landscape simulation also accelerates in the last three decades, to an intermediate increase rate,
such that by 2100 it is about $2.4\,\mathrm{m}$ and thus lies within the range spanned by the two single-tile simulations under contrasting
hydrological conditions, but closer to the poorly-drained simulation.

310   *Ground subsidence:* While ground subsidence starts already after about two decades in the landscape simulation, no subsi-
dence occurs until about 2060 in both single-tile simulations (Fig. 5 c). The accumulated mean ground subsidence in the land-
scape simulation reaches about $0.3\,\mathrm{m}$ in 2060, and accelerates afterwards, reaching about $1.8\,\mathrm{m}$ in 2100. Ground subsidence in
the single tile simulations sets on abruptly around the year 2070 and is about three times faster in the poorly-drained than in
the well-drained simulation. By 2100, it reaches about $2.0\,\mathrm{m}$ in the poorly-drained case, and about $0.7\,\mathrm{m}$ in the well-drained,
315   such that the landscape simulation is within the range spanned by the single-tile simulations, but closer to the poorly-drained
simulation.

3.2.2   Simulations with micro-scale heterogeneity reflecting ice-wedge polygons

Maximum thawed ground: All simulations with polygons as the micro-scale representation, had a similar maximum thawed
ground extent of about $0.5\,\mathrm{m}$ in 2000 (Fig. 5 b). This amount increased steadily until about 2060, but at different rates among the
320   three simulations. The permafrost thaw rate is fastest for the poorly-drained single-polygon where the maximum thawed ground
reaches about $1.2\,\mathrm{m}$ in 2060, and it is slowest for the well-drained single-polygon for which it reaches about $0.7\,\mathrm{m}$ by the same
time. After 2060 the increase in the simulated thawed ground extents becomes faster in the single-tile simulations. By 2100
it reaches about $1.2\,\mathrm{m}$ in the well-drained simulation, and more than $4\,\mathrm{m}$ in the poorly-drained simulation. The mean thawed
ground in the polygon landscape simulation lies within the range spanned by the two single-polygon simulations throughout
325   the 21st century. However, during the last three to four decades, the increase does not accelerate such that it aligns more with
the well-drained simulation, reaching a value of about $1.3\,\mathrm{m}$ by 2100. As a general pattern, thaw depths are consistently larger
in the single-polygon simulations than in the single-tile simulations with homogeneous micro-scale representation. In contrast,
the thaw depths in the polygon landscape simulation are consistently lower than in the homogeneous landscape simulation,
particularly during the last three decades.

330   *Ground subsidence:* Excess ice melt and associated ground subsidence occur within the first decade in the poorly-drained
single-polygon simulation and in the polygon landscape simulation, while the ground does not subside before 2050 in the
poorly-drained polygon simulation (Fig. 5 d). As for the thawed ground discussed above, mean ground subsidence in the
polygon landscape simulation is constrained by the two single-polygon simulations. By 2060, mean ground subsidence in the
polygon landscape reaches about $0.4\,\mathrm{m}$. During the last four decades, ground subsidence sets in and proceeds in the well-
335   drained single-polygon simulation, reaching a value of about $1.0\,\mathrm{m}$ by 2100. In the poorly-drained single-polygon simulation,
subsidence rates are about three times faster, reaching more than $3\,\mathrm{m}$ by 2100. In the polygon landscape simulation, subsidence
rates do not accelerate markedly during the last decades and the mean total subsidence is close to that of the well-drained
polygon by 2100. A similar general pattern as for the thaw depths is found for the accumulated subsidence. Simulated ground

subsidence in the single-polygon simulations consistently exceeds the respective projections of the homogeneous single-tile

340 simulations, while the mean ground subsidence by 2100 is substantially larger in the homogeneous landscape than in the polygon landscape.

4 Discussion

4.1 Simulating landscape degradation pathways under consideration of micro- and meso-scale heterogeneity

The multi-scale tiling approach employed in this study (see Section 2.3.2) facilitates the simulation of degradation pathways

345 of ice-rich permafrost landscapes in response to a warming climate, under consideration of feedback processes emerging from heterogeneities and lateral fluxes on subgrid-scales. The most idealized cases considered were one-tile simulations without heterogeneities on the micro- or meso-scale (Fig. 2 a; Fig. 3 first and fifth column). Depending on the hydrological boundary conditions, these simulations reflect different real-world cases. Under well-drained conditions, the simulation reflects an "upland" setting for which steady ground subsidence was projected under RCP8.5 during the second half of the twenty-first

350 century and no surface water can form. If drainage was precluded, the simulations projected the formation of a thaw lake to occur during the second half of the twenty-first century. While these model configurations correspond to the two cases considered by Westermann et al. (2016), the response of the presented simulations in this study differs both qualitatively and quantitatively. Overall, the projected permafrost degradation in this study is considerably lower than in the projections of Westermann et al. (2016) who assumed similar excess ice contents and used the same meteorological forcing data. This can most likely be

355 attributed to the inclusion of a water balance into CryoGrid 3 (Nitzbon et al., 2019; Martin et al., 2019).

These simple cases, however, do not reflect a lot of processes observed in real-word landscapes, such as dynamically changing hydrological conditions due to lateral water fluxes. These have been taken into account in the homogeneous landscape setting (Fig. 2 c, 3 second to fourth column). Compared to the single-tile cases, the landscape evolution is affected by lateral interactions between different parts of the simulated landscape. Surface water formation in the inland parts is projected

360 to occur earlier than in poorly-drained single-tile case, which can be attributed to very poor drainage along the low-gradient slope. Furthermore, the subsiding outer part causes a gradual drainage of the thaw lake in the inner part, such that it is substantially more shallow by the end of the simulation than in the poorly-drained single-tile case. Shallow water bodies favor bottom-freezing, such that the gradual lake drainage would constitute a stabilizing feedback on the ground thermal regime in the simulations. However, real world thaw lakes are also known to drain "catastrophically", for example, upon the incision of a

365 thermo-erosional gully as a result of either gully growth or lake expansion (Jones et al., 2011; Kessler et al., 2012). Both are a consequence of lateral erosion which is not represented in our model at the meso-scale. Besides feedbacks through meso-scale water fluxes, previous modeling studies demonstrated that the stability and the thermal regime of permafrost in the vicinity of thaw lakes is affected by meso-scale heat fluxes from taliks forming underneath the lakes (Rowland et al., 2011; Langer et al., 2016). These effects have not been considered in this study.

370 As suggested by several studies (Nitzbon et al., 2019; Abolt et al., 2020), the degradation pathways of ice-rich permafrost become more involved, if the micro-scale heterogeneity associated with ice-wedge polygons is taken into account, for example

due to the lateral rerouting of surface and subsurface water according to the micro-scale topography. Here, we took into account micro-scale lateral fluxes of heat, water, snow, and sediment (see Fig. 2 b). The single-polygon simulations in this study correspond to the simulations for "Holocence Deposits" presented in Nitzbon et al. (2020) in terms of the ground ice distribution and the meteorological forcing data. Consequently, qualitatively identical landscape evolution pathways have been simulated (Fig. 4 first and fifth column). Under well-drained conditions the low-centred polygons evolve into high-centred polygons with a pronounced relief, while a deep thaw lake underlain by a talik has been simulated to from, under poorly-drained conditions. These two cases span a wide range of uncertainty in terms of projected permafrost degradation.

The simulation of the polygon landscape that takes into account meso-scale water fluxes (Fig. 2 d, Fig. 4 second to fourth column) has been conducted to provide a more realistic representation of heterogeneity in ice-rich terrain, and it revealed a subtle transient landscape evolution in response to climate warming. In that simulation surface water ponds early in the inland parts of the landscape, associated with initial ice-wedge degradation. The degradation is slowed down, however, by lateral transport of sediment (slumping) from the rims into the troughs (see Fig. 4 b–c, fourth column), such that the high-centred polygons are stabilized temporarily. During the second half of the twenty-first century, rapid ice-wedge degradation occurs in the outer part of the landscape, and the entire landscape drains as a consequence. Overall, the simulation reflects a transition from a low-gradient landscape of undegraded low-centered polygons to well-drained high-centered polygons within less than a century. This transient simulation thus corresponds to the schematic landscape evolution depicted by Liljedahl et al. (2016). This constitutes a significant improvement over the previous versions of the model (Nitzbon et al., 2019, 2020), for which it was not possible to simulate this type of landscape dynamics. It should further be noted that the simulated shifts in the subsurface hydrological regime have important consequences for whether the decomposition of soil organic carbon occurs under aerobic or anaerobic conditions (Lara et al., 2015; Schuur et al., 2015; Schädel et al., 2016; Knoblauch et al., 2018).

4.2 Constraining the response of ice-rich permafrost to a warming climate

Depending on the inclusion of landscape heterogeneities at different scales, the presented simulations reveal very different permafrost degradation trajectories (Fig. 5). Irrespective of the representation of micro-scale heterogeneity, the simulations under well-drained and poorly-drained conditions provide outer boundaries in terms of thaw and subsidence for the landscape simulations. The landscape-scale mean of the three-tile simulation without representation of micro-scale heterogeneity, revealed permafrost degradation trajectories which proceed slower than the poorly-drained case, but align closer to it than to the well-drained case. However, when the micro-scale was represented as ice-wedge polygons, the resulting degradation trajectories aligned closer to the well-drained case, as a consequence of the drainage network formation described in the previous section. The simulations thus indicate that the overall (landscape-mean) permafrost degradation, is crucially affected by small-scale heterogeneities, and that model projections have to be considered with care in light of these complexities. Hence, our simulations do not allow a final judgment with respect to whether the formation of new thaw lakes and taliks, or the formation of new drainage systems will dominate the evolution of real-world permafrost lowlands under a warming climate. For a more realistic assessment of the most likely response of ice-rich permafrost to climate warming, additional configurations than the two exemplary cases presented here would need to be considered, for example by incorporating also different meso-scale topologies

which could correspond to different catchment geometries. This could also help to test the hypotheses on thaw lake abundance which underlie other models' projections of greenhouse gas emissions from thermokarst terrain (Schneider von Deimling et al., 2015; Walter Anthony et al., 2018).

Our simulations further suggest, that abrupt degradation of ice-rich permafrost across entire landscapes is less likely than

410 spatially distributed and gradual degradation dynamics. When either micro- or meso-scale heterogeneities (or both) are taken into account in the simulations, the projected degradation trajectories are more gradual and steady than in the overly simplistic one-tile simulations (Fig. 5). The one-tile simulations show a relatively abrupt onset of subsidence and thaw-depth increase, and similar abrupt changes in ground thermal and hydrological regimes have been found using similarly simplistic model setup (Teufel and Sushama, 2019). We interpret our findings to suggest that abrupt responses of permafrost terrain to climate

415 warming may occur locally, but are not likely at regional or even global scales.

4.3 Simulating the cyclic evolution of ice wedges and thaw lakes in thermokarst terrain

It has been suggested that thermokarst terrain evolves in a cyclic manner on centennial-to-millennial timescales. For example, the cycles of degradation and stabilization have been suggested to describe the evolution of ice wedges (Jorgenson et al., 2006, 2015; Kanevskiy et al., 2017) on these time scales. Similarly, but at a larger spatial scale, the cyclic evolution of thaw lakes

420 has been hypothesized (Billings and Peterson, 1980) (see Grosse et al. (2013) for a review of the hypothesis). While we do not want to discuss to which extent ice-rich permafrost landscapes have been evolving or are evolving according to these models, we would like to point out that the model framework presented in this study, is in principle able to capture a wide range of the processes involved in these cycles. Figure 6 provides a schematic of the cyclic evolution of thermokarst terrain based and highlights the capacities of our model to simulate different pathways.

425 The initial and advanced degradation of ice wedges and the associated transition from low-centered to high-centered polygons was captured by the model setup by Nitzbon et al. (2019). Nitzbon et al. (2020) complemented this by the stabilizing of ice wedges due to sediment accumulation in the troughs, and also showed that it is possible to simulate ice-wedge collapse and thaw lake formation in response to climate warming scenarios. The simulations with representation of landscape heterogeneity and lateral water fluxes at the meso-scale, which are presented in this study, allow to capture further feedbacks. First, the

430 formation of efficient drainage pathways through degrading ice-wedge networks, as depicted by Liljedahl et al. (2016), was qualitatively captured by the simulation using the polygon landscape setup (Fig. 2 d). While this drainage did not completely interrupt the ice-wedge degradation (as indicated in Fig. 6), it did lead to a significantly slower degradation compared to the simulations without meso-scale heterogeneity (Fig. 5 b,c). Second, representing meso-scale lateral water fluxes (Fig. 2 c,d) enables our model in principle to simulate the drainage of thaw lakes, which would result in the exposure of unfrozen ground

435 (talik) to the atmosphere. While it is not possible to simulate the catastrophic drainage of lakes as discussed above, gradual subsidence of the terrain surrounding the thaw lake, can lead to its gradual drainage on longer timescales than considered here. It is further likely that using a model setup with a more complex meso-scale landscape topology, could result in more rapid drainage.
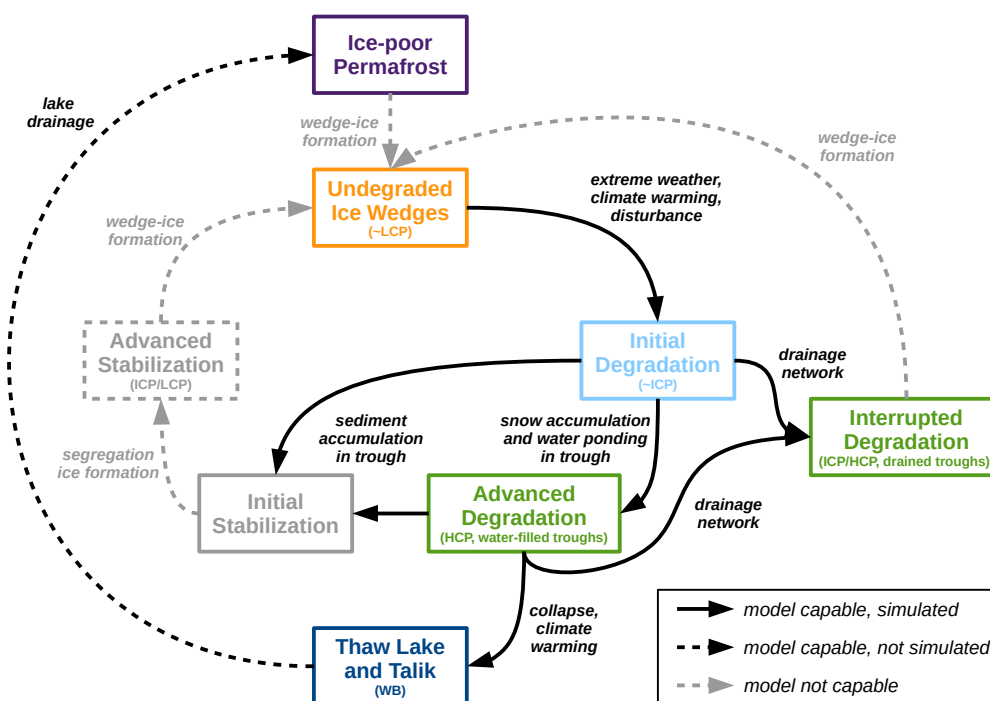
Figure 6. Schematic depiction of pathways of ice-rich permafrost landscape evolution as simulated within the presented model framework. The "inner" cycle reflects the cyclic evolution of ice wedges as described by Kanevskiy et al. (2017). The outer cycle involving the thaw lake stage reflects the thaw lake cylce as hypothesized by Billings and Peterson (1980). Formation of excess ice is lacking in the model such that the full cycles cannot be simulated. Adapted from Jorgenson et al. (2015) and Nitzbon et al. (2019).

As indicated in Fig. 6, several processes are not represented in our model, such that it cannot capture the full cycles of ice-rich

440   permafrost evolution. In order to represent the initial stabilization of ice wedges more realistically, further ecological processes like vegetation succession and organic matter formation would need to be represented Jorgenson et al. (2015); Kanevskiy et al. (2017). However, lateral sediment transport into the troughs captures this stage to a certain extent. The advanced stabilization of ice wedges, involves the formation of ice-rich layers consisting of segregation ice above the massive ice wedge. The process of ice-segregation would require a more sophisticated subsurface hydrology scheme, representing the migration of liquid pore

445   water towards the freezing front, as well as vertical displacement of sediment resulting from frost heave (O'Neill et al., 2019). Finally, and probably most importantly, the formation of wedge ice is not yet represented in the model, which is, however, necessary to from the initial stage of undegraded ice wedges from various other evolutionary stages (Fig. 6). In contrast to the formation of segregation ice, wedge-ice formation involves both vertical and horizontal processes, which presupposes the formation of frost cracks due to mechanical stress, which in turn is controlled by climatic conditions at the ground surface and

450   at the top of permafrost (Lachenbruch, 1962).

21

The Cryosphere

Discussions

Open Access

EGU

5 Conclusions

In the present study, we employed a multi-scale hierarchical tiling approach in the CryoGrid 3 numerical model to assess the response of ice-rich permafrost landscapes in northeast Siberia to a warming climate. Specifically, we explored the sensitivity of the model simulations to different representations of micro- and meso-scale heterogeneities and lateral fluxes. From the results of this study, we draw the following conclusions:

1. Representing meso-scale heterogeneity and lateral fluxes allows to represent a wider range of permafrost degradation pathways under a warming climate, including, e.g., the large-scale drainage initiated by ice-wedge degradation or the dynamic formation and drainage of thaw lakes.

2. Representing micro-scale heterogeneity and lateral fluxes associated with ice-wedge polygons affects the timing and the rate of permafrost thaw, as well as the hydrological response to climate warming. In particular, the drainage network that evolves when ice wedges melt, favors large-scale drainage of the landscape and can impede new thaw lake formation.

3. Incorporating subgrid-scale heterogneities and lateral fluxes using a multi-scale tiling approach allows to constrain uncertainties in the response of ice-rich permafrost landscapes to a warming climate. The response of permafrost is more gradual in simulations representing subgrid-scale processes compared to abrupt changes projected by simple one-dimensional representations. Micro-scale lateral sediment transport is an example for a stabilizing process in ice-wedge terrain, which moderates rapid thaw processes.

4. Irrespective of uncertainties associated with future climate forcing, robust projections of the response of permafrost to climate change require solid knowledge on the distribution of (excess) ground ice on different scales, as well as information on topographic conditions (i.e., slope, connectivity, topology of drainage systems, etc.) which govern the meso-scale hydrology.

In summary, our work provides further constraints on projections of future permafrost degradation and landscape evolution in ice-rich lowland tundra of northeast Siberia, and contributes to the development of realistic and computationally efficient representations of the permafrost region in land surface schemes of ESMs.

6 Outlook

The presented modeling framework allows to reflect a multitude of transient degradation pathways and feedback processes in ice-rich permafrost landscapes and can thus contribute to an improved understanding of permafrost evolution in response to changing climatic conditions. In order to evaluate and validate the process representations in the model further, a next step would be to apply the model to different sites across the permafrost region, provided the necessary field data to set up and evaluate the simulations. Depending on site-specific or regional circumstances, the model would need to be extended by further parameterizations. For example, Zweigel et al. (2020) introduced an improved snow scheme into the CryoGrid model,

in order to capture more complex snow dynamics at a high-Arctic permafrost site on Svalbard. Such case studies employing field data for validation will contribute to build confidence in permafrost models' projections in general, and in the CryoGrid framework in particular.

Besides such site-specific case studies, our model provides the opportunity to assess the response of (ice-rich) permafrost
485 on regional to pan-Arctic scales. Given the sensitivity of permafrost thaw dynamics to subgrid-scale heterogeneity and lateral fluxes, we suggest that a combination of tiling concepts as presented in this study, and statistical methods such as model ensembles could provide more robust and realistic projections. Facilitating further abstraction of real-world landscapes in numerical models, methods from graph theory (i.e., network theory) could be explored as a potential technique to represent lateral processes such water transport across spatial scales (e.g., Zuecco et al. (2019)). The tiling setups depicted in Fig. 2
490 correspond to simple graph topologies.

Finally, remotely-sensed data that provide information on topographic and hydrological characteristics, such as the distance to a downstream drainage point, the upstream catchment area, or the slope, are an opportunity to inform and improve numerical model assessments. In addition, such data can be used to evaluate model performance under recent climatic conditions. For example, various recent studies addressed the mapping of ice-wedge polygon geomorphology based on high-resolution DEMs
495 (e.g., Kartoziia (2019)), and machine-learning techniques are being developed to map ice-wedge polygons in increasingly large areas of hundreds of square kilometers (Abolt et al., 2019; Zhang et al., 2018; Abolt and Young, 2020; Zhang et al., 2020). In the future, time series of such high-resolution elevation data of ice-rich terrain, would allow better evaluation and improvement of numerical models like CryoGrid 3 that simulated elevation changes due to melting of excess ice (e.g., Wagner et al. (2018)). It is thus desirable, that high-resolution elevation models would become a key observable of long-term permafrost monitoring
500 efforts, similar to the systematic monitoring of ground temperatures and active layer depths.

Code availability. The model code used and settings used for the simulations is available from https://github.com/CryoGrid/CryoGrid3/tree/xice_mpi_polygon_landscape. It will be permanently deposited upon acceptance of the manuscript. The code is published under the GNU General Public License v3.0.

Appendix A: Calculation of lateral surface and subsurface water fluxes

505 Lateral water fluxes (q_α [m s^{-1}]) to a tile α from hydrologically connected tiles $\beta \in \mathcal{N}(\alpha)$ were calculated as the sum of surface and subsurface contributions:

$$q_\alpha = q_\alpha^{\text{surf}} + q_\alpha^{\text{subs}} \tag{A1}$$

Following Darcy's law, both surface and subsurface fluxes were assumed to be proportional to a gradient in the hydraulic heads (h), but assuming different saturated hydraulic conductivities ($K^{\text{surf/subs}}$) and contact heights ($H^{\text{surf/subs}}$):

510
$$q_\alpha^{\text{surf}} = \frac{1}{A_\alpha} \sum_{\beta \in \mathcal{N}(\alpha)} K_{\alpha\beta}^{\text{surf}} \frac{h_\beta - h_\alpha}{D_{\alpha\beta}} H_{\alpha\beta}^{\text{surf}} L_{\alpha\beta} \tag{A2}$$

$$q_\alpha^{\text{subs}} = \frac{1}{A_\alpha} \sum_{\beta \in \mathcal{N}(\alpha)} K_{\alpha\beta}^{\text{subs}} \frac{h_\beta - h_\alpha}{D_{\alpha\beta}} H_{\alpha\beta}^{\text{subs}} L_{\alpha\beta} \tag{A3}$$

where D is the distance between the tiles and L the contact length which have been introduced in Section 2.4.3. The hydraulic head of each tile was identified with the water table elevation (w), or the frost table elevation (f) if no water table was present ($h = \max(w, f)$). The contact heights for the surface and subsurface fluxes were obtained as follows:

515
$$H_{\alpha\beta}^{\text{surf}} = \max\left(0, h^{\text{max}} - \max\left(s^{\text{max}}, f^{\text{max}}\right)\right) \tag{A4}$$

$$H_{\alpha\beta}^{\text{subs}} = \max\left(0, \min\left(h^{\text{max}} - f^{\text{max}}, s^{\text{max}} - f^{\text{max}}\right)\right) \tag{A5}$$

where $h^{\text{max}} = \max(h_\alpha, h_\beta)$ is the maximum hydraulic head, $s^{\text{max}} = \max(s_\alpha, s_\beta)$ is the maximum soil surface elevation, and $f^{\text{max}} = \max(f_\alpha, f_\beta)$ is the maximum frost table elevation of the two involved tiles. As described in Nitzbon et al. (2019), lateral water fluxes were only applied, when both tiles were snow-free and the uppermost soil grid cell unfrozen.

The Cryosphere
Discussions

Open Access

EGU

References

Aas, K. S., Martin, L., Nitzbon, J., Langer, M., Boike, J., Lee, H., Berntsen, T. K., and Westermann, S.: Thaw processes in ice-rich permafrost
530   landscapes represented with laterally coupled tiles in a land surface model, The Cryosphere, 13, 591–609, https://doi.org/10.5194/tc-13-
591-2019, 2019.

Abolt, C. J. and Young, M. H.: High-resolution mapping of spatial heterogeneity in ice wedge polygon geomorphology near Prudhoe Bay,
Alaska, Scientific Data, 7, 1–7, https://doi.org/10.1038/s41597-020-0423-9, 2020.

Abolt, C. J., Young, M. H., Atchley, A. L., and Harp, D. R.: Microtopographic control on the ground thermal regime in ice wedge polygons,
535   The Cryosphere, 12, 1957–1968, https://doi.org/10.5194/tc-12-1957-2018, 2018.

Abolt, C. J., Young, M. H., Atchley, A. L., and Wilson, C. J.: Brief communication: Rapid machine-learning-based extrac-
tion and measurement of ice wedge polygons in high-resolution digital elevation models, The Cryosphere, 13, 237–245,
https://doi.org/https://doi.org/10.5194/tc-13-237-2019, 2019.

Abolt, C. J., Young, M. H., Atchley, A. L., Harp, D. R., and Coon, E. T.: Feedbacks Between Surface Deformation and Permafrost Degra-
540   dation in Ice Wedge Polygons, Arctic Coastal Plain, Alaska, Journal of Geophysical Research: Earth Surface, 125, e2019JF005 349,
https://doi.org/10.1029/2019JF005349, 2020.

AMAP: Snow, Water, Ice and Permafrost in the Arctic (SWIPA) 2017, Arctic Monitoring and Assessment Programme, Oslo, Norway, oCLC:
1038467657, 2017.

Andresen, C. G., Lawrence, D. M., Wilson, C. J., McGuire, A. D., Koven, C., Schaefer, K., Jafarov, E., Peng, S., Chen, X., Gouttevin, I.,
545   Burke, E., Chadburn, S., Ji, D., Chen, G., Hayes, D., and Zhang, W.: Soil moisture and hydrology projections of the permafrost region – a
model intercomparison, The Cryosphere, 14, 445–459, https://doi.org/https://doi.org/10.5194/tc-14-445-2020, 2020.

Billings, W. D. and Peterson, K. M.: Vegetational Change and Ice-Wedge Polygons through the Thaw-Lake Cycle in Arctic Alaska, Arctic
and Alpine Research, 12, 413–432, https://doi.org/10.1080/00040851.1980.12004204, 1980.

Biskaborn, B. K., Smith, S. L., Noetzli, J., Matthes, H., Vieira, G., Streletskiy, D. A., Schoeneich, P., Romanovsky, V. E., Lewkowicz, A. G.,
550   Abramov, A., Allard, M., Boike, J., Cable, W. L., Christiansen, H. H., Delaloye, R., Diekmann, B., Drozdov, D., Etzelmüller, B., Grosse,
G., Guglielmin, M., Ingeman-Nielsen, T., Isaksen, K., Ishikawa, M., Johansson, M., Johannsson, H., Joo, A., Kaverin, D., Kholodov, A.,
Konstantinov, P., Kröger, T., Lambiel, C., Lanckman, J.-P., Luo, D., Malkova, G., Meiklejohn, I., Moskalenko, N., Oliva, M., Phillips, M.,
Ramos, M., Sannel, A. B. K., Sergeev, D., Seybold, C., Skryabin, P., Vasiliev, A., Wu, Q., Yoshikawa, K., Zheleznyak, M., and Lantuit,
H.: Permafrost is warming at a global scale, Nature Communications, 10, 264, https://doi.org/10.1038/s41467-018-08240-4, 2019.

555   Boike, J., Wille, C., and Abnizova, A.: Climatology and summer energy and water balance of polygonal tundra in the Lena River Delta,
Siberia, Journal of Geophysical Research, 113, https://doi.org/10.1029/2007JG000540, 2008.

Boike, J., Kattenstroth, B., Abramova, K., Bornemann, N., Chetverova, A., Fedorova, I., Fröb, K., Grigoriev, M., Grüber, M., Kutzbach,
L., Langer, M., Minke, M., Muster, S., Piel, K., Pfeiffer, E.-M., Stoof, G., Westermann, S., Wischnewski, K., Wille, C., and Hubberten,
H.-W.: Baseline characteristics of climate, permafrost and land cover from a new permafrost observatory in the Lena River Delta, Siberia
560   (1998–2011), Biogeosciences, 10, 2105–2128, https://doi.org/10.5194/bg-10-2105-2013, 2013.

Boike, J., Nitzbon, J., Anders, K., Grigoriev, M., Bolshiyanov, D., Langer, M., Lange, S., Bornemann, N., Morgenstern, A., Schreiber,
P., Wille, C., Chadburn, S., Gouttevin, I., Burke, E., and Kutzbach, L.: A 16-year record (2002–2017) of permafrost, active-layer,
and meteorological conditions at the Samoylov Island Arctic permafrost research site, Lena River delta, northern Siberia: an op-

portunity to validate remote-sensing data and land surface, snow, and permafrost models, Earth System Science Data, 11, 261–299,
565   https://doi.org/10.5194/essd-11-261-2019, 2019.

Farquharson, L. M., Romanovsky, V. E., Cable, W. L., Walker, D. A., Kokelj, S. V., and Nicolsky, D.: Climate Change Drives Widespread and
    Rapid Thermokarst Development in Very Cold Permafrost in the Canadian High Arctic, Geophysical Research Letters, 46, 6681–6689,
    https://doi.org/10.1029/2019GL082187, 2019.

Fortier, D., Allard, M., and Shur, Y.: Observation of rapid drainage system development by thermal erosion of ice wedges on Bylot Island,
570   Canadian Arctic Archipelago, Permafrost and Periglacial Processes, 18, 229–243, https://doi.org/10.1002/ppp.595, 2007.

Godin, E., Fortier, D., and Coulombe, S.: Effects of thermo-erosion gullying on hydrologic flow networks, discharge and soil loss, Environ-
    mental Research Letters, 9, 105 010, https://doi.org/10.1088/1748-9326/9/10/105010, 2014.

Gouttevin, I., Langer, M., Löwe, H., Boike, J., Proksch, M., and Schneebeli, M.: Observation and modelling of snow at a polygonal tundra
    permafrost site: spatial variability and thermal implications, The Cryosphere, 12, 3693–3717, https://doi.org/https://doi.org/10.5194/tc-
575   12-3693-2018, 2018.

Grosse, G., Jones, B., and Arp, C.: 8.21 Thermokarst Lakes, Drainage, and Drained Basins, in: Treatise on Geomorphology, edited by
    Shroder, J. F., pp. 325–353, Academic Press, San Diego, https://doi.org/10.1016/B978-0-12-374739-6.00216-5, 2013.

Hjort, J., Karjalainen, O., Aalto, J., Westermann, S., Romanovsky, V. E., Nelson, F. E., Etzelmüller, B., and Luoto, M.: Degrading permafrost
    puts Arctic infrastructure at risk by mid-century, Nature Communications, 9, https://doi.org/10.1038/s41467-018-07557-4, 2018.

580   Jafarov, E. E., Coon, E. T., Harp, D. R., Wilson, C. J., Painter, S. L., Atchley, A. L., and Romanovsky, V. E.: Modeling the role of preferential
    snow accumulation in through talik development and hillslope groundwater flow in a transitional permafrost landscape, Environmental
    Research Letters, 13, 105 006, https://doi.org/10.1088/1748-9326/aadd30, 2018.

Jones, B. M., Grosse, G., Arp, C. D., Jones, M. C., Anthony, K. M. W., and Romanovsky, V. E.: Modern thermokarst lake dynam-
    ics in the continuous permafrost zone, northern Seward Peninsula, Alaska, Journal of Geophysical Research: Biogeosciences, 116,
585   https://doi.org/10.1029/2011JG001666, 2011.

Jorgenson, M. T., Shur, Y. L., and Pullman, E. R.: Abrupt increase in permafrost degradation in Arctic Alaska, Geophysical Research Letters,
    33, https://doi.org/10.1029/2005GL024960, 2006.

Jorgenson, M. T., Kanevskiy, M., Shur, Y., Moskalenko, N., Brown, D. R. N., Wickland, K., Striegl, R., and Koch, J.: Role of ground ice
    dynamics and ecological feedbacks in recent ice wedge degradation and stabilization, Journal of Geophysical Research: Earth Surface,
590   120, 2280–2297, https://doi.org/10.1002/2015JF003602, 2015.

Kanevskiy, M., Shur, Y., Jorgenson, T., Brown, D. R., Moskalenko, N., Brown, J., Walker, D. A., Raynolds, M. K., and Buchhorn, M.:
    Degradation and stabilization of ice wedges: Implications for assessing risk of thermokarst in northern Alaska, Geomorphology, 297,
    20–42, https://doi.org/10.1016/j.geomorph.2017.09.001, 2017.

Kartoziia, A.: Assessment of the Ice Wedge Polygon Current State by Means of UAV Imagery Analysis (Samoylov Island, the Lena Delta),
595   Remote Sensing, 11, 1627, https://doi.org/10.3390/rs11131627, 2019.

Kessler, M. A., Plug, L. J., and Anthony, K. M. W.: Simulating the decadal- to millennial-scale dynamics of morphology and se-
    questered carbon mobilization of two thermokarst lakes in NW Alaska, Journal of Geophysical Research: Biogeosciences, 117, G00M06,
    https://doi.org/10.1029/2011JG001796, 2012.

Knoblauch, C., Beer, C., Liebner, S., Grigoriev, M. N., and Pfeiffer, E.-M.: Methane production as key to the greenhouse gas budget of
600   thawing permafrost, Nature Climate Change, 8, 309–312, https://doi.org/10.1038/s41558-018-0095-z, 2018.

Kokelj, S. V. and Jorgenson, M. T.: Advances in Thermokarst Research, Permafrost and Periglacial Processes, 24, 108–119, https://doi.org/10.1002/ppp.1779, 2013.

Lachenbruch, A. H.: Mechanics of Thermal Contraction Cracks and Ice-Wedge Polygons in Permafrost, in: Geological Society of America Special Papers, vol. 70, pp. 1–66, Geological Society of America, https://doi.org/10.1130/SPE70-p1, 1962.

605 Langer, M., Westermann, S., Muster, S., Piel, K., and Boike, J.: The surface energy balance of a polygonal tundra site in northern Siberia - Part 2: Winter, The Cryosphere, 5, 509–524, https://doi.org/10.5194/tc-5-509-2011, 2011a.

Langer, M., Westermann, S., Muster, S., Piel, K., and Boike, J.: The surface energy balance of a polygonal tundra site in northern Siberia - Part 1: Spring to fall, The Cryosphere, 5, 151–171, https://doi.org/10.5194/tc-5-151-2011, 2011b.

Langer, M., Westermann, S., Boike, J., Kirillin, G., Grosse, G., Peng, S., and Krinner, G.: Rapid degradation of permafrost underneath
610 waterbodies in tundra landscapes—Toward a representation of thermokarst in land surface models, Journal of Geophysical Research: Earth Surface, 121, 2446–2470, https://doi.org/10.1002/2016JF003956, 2016.

Lara, M. J., McGuire, A. D., Euskirchen, E. S., Tweedie, C. E., Hinkel, K. M., Skurikhin, A. N., Romanovsky, V. E., Grosse, G., Bolton, W. R., and Genet, H.: Polygonal tundra geomorphological change in response to warming alters future CO2 and CH4 flux on the Barrow Peninsula, Global Change Biology, 21, 1634–1651, https://doi.org/10.1111/gcb.12757, 2015.

615 Lawrence, D. M., Slater, A. G., and Swenson, S. C.: Simulation of Present-Day and Future Permafrost and Seasonally Frozen Ground Conditions in CCSM4, Journal of Climate, 25, 2207–2225, https://doi.org/10.1175/JCLI-D-11-00334.1, 2012.

Lee, H., Swenson, S. C., Slater, A. G., and Lawrence, D. M.: Effects of excess ground ice on projections of permafrost in a warming climate, Environmental Research Letters, 9, 124 006, https://doi.org/10.1088/1748-9326/9/12/124006, 2014.

Liljedahl, A. K., Boike, J., Daanen, R. P., Fedorov, A. N., Frost, G. V., Grosse, G., Hinzman, L. D., Iijma, Y., Jorgenson, J. C., Matveyeva,
620 N., Necsoiu, M., Raynolds, M. K., Romanovsky, V. E., Schulla, J., Tape, K. D., Walker, D. A., Wilson, C. J., Yabuki, H., and Zona, D.: Pan-Arctic ice-wedge degradation in warming permafrost and its influence on tundra hydrology, Nature Geoscience, 9, 312–318, https://doi.org/10.1038/ngeo2674, 2016.

Martin, L. C. P., Nitzbon, J., Aas, K. S., Etzelmüller, B., Kristiansen, H., and Westermann, S.: Stability Conditions of Peat Plateaus and Palsas in Northern Norway, Journal of Geophysical Research: Earth Surface, https://doi.org/10.1029/2018JF004945, 2019.

625 Muster, S., Langer, M., Heim, B., Westermann, S., and Boike, J.: Subpixel heterogeneity of ice-wedge polygonal tundra: a multi-scale analysis of land cover and evapotranspiration in the Lena River Delta, Siberia, Tellus B: Chemical and Physical Meteorology, 64, 17 301, https://doi.org/10.3402/tellusb.v64i0.17301, 2012.

Nitzbon, J., Langer, M., Westermann, S., Martin, L., Aas, K. S., and Boike, J.: Pathways of ice-wedge degradation in polygonal tundra under different hydrological conditions, The Cryosphere, 13, 1089–1123, https://doi.org/10.5194/tc-13-1089-2019, 2019.

630 Nitzbon, J., Westermann, S., Langer, M., Martin, L. C. P., Strauss, J., Laboor, S., and Boike, J.: Fast response of cold ice-rich permafrost in northeast Siberia to a warming climate, Nature Communications, 11, 2201, https://doi.org/10.1038/s41467-020-15725-8, 2020.

O'Neill, H. B., Wolfe, S. A., and Duchesne, C.: New ground ice maps for Canada using a paleogeographic modelling approach, The Cryosphere, 13, 753–773, https://doi.org/https://doi.org/10.5194/tc-13-753-2019, 2019.

Painter, S. L., Coon, E. T., Atchley, A. L., Berndt, M., Garimella, R., Moulton, J. D., Svyatskiy, D., and Wilson, C. J.: Integrated sur-
635 face/subsurface permafrost thermal hydrology: Model formulation and proof-of-concept simulations, Water Resources Research, 52, 6062–6077, https://doi.org/10.1002/2015WR018427, 2016.

Rowland, J. C., Jones, C. E., Altmann, G., Bryan, R., Crosby, B. T., Hinzman, L. D., Kane, D. L., Lawrence, D. M., Mancino, A., Marsh, P., McNamara, J. P., Romanvosky, V. E., Toniolo, H., Travis, B. J., Trochim, E., Wilson, C. J., and Geernaert, G. L.:

27

Arctic Landscapes in Transition: Responses to Thawing Permafrost, Eos, Transactions American Geophysical Union, 91, 229–230,
640   https://doi.org/10.1029/2010EO260001, 2010.

Rowland, J. C., Travis, B. J., and Wilson, C. J.: The role of advective heat transport in talik development beneath lakes and ponds in
discontinuous permafrost, Geophysical Research Letters, 38, https://doi.org/10.1029/2011GL048497, 2011.

Schneider von Deimling, T., Grosse, G., Strauss, J., Schirrmeister, L., Morgenstern, A., Schaphoff, S., Meinshausen, M., and Boike, J.:
Observation-based modelling of permafrost carbon fluxes with accounting for deep carbon deposits and thermokarst activity, Biogeo-
645   sciences, 12, 3469–3488, https://doi.org/10.5194/bg-12-3469-2015, 2015.

Schuur, E. A. and Mack, M. C.: Ecological Response to Permafrost Thaw and Consequences for Local and Global Ecosystem Services,
Annual Review of Ecology, Evolution, and Systematics, 49, 279–301, https://doi.org/10.1146/annurev-ecolsys-121415-032349, 2018.

Schuur, E. A. G., McGuire, A. D., Schädel, C., Grosse, G., Harden, J. W., Hayes, D. J., Hugelius, G., Koven, C. D., Kuhry, P., Lawrence,
D. M., Natali, S. M., Olefeldt, D., Romanovsky, V. E., Schaefer, K., Turetsky, M. R., Treat, C. C., and Vonk, J. E.: Climate change and the
650   permafrost carbon feedback, Nature, 520, 171–179, https://doi.org/10.1038/nature14338, 2015.

Schwamborn, G., Rachold, V., and Grigoriev, M. N.: Late Quaternary sedimentation history of the Lena Delta, Quaternary International, 89,
119–134, https://doi.org/10.1016/S1040-6182(01)00084-2, 2002.

Schädel, C., Bader, M. K.-F., Schuur, E. A. G., Biasi, C., Bracho, R., Čapek, P., De Baets, S., Diáková, K., Ernakovich, J., Estop-Aragones,
C., Graham, D. E., Hartley, I. P., Iversen, C. M., Kane, E., Knoblauch, C., Lupascu, M., Martikainen, P. J., Natali, S. M., Norby, R. J.,
655   O'Donnell, J. A., Chowdhury, T. R., Šantrůčková, H., Shaver, G., Sloan, V. L., Treat, C. C., Turetsky, M. R., Waldrop, M. P., and Wick-
land, K. P.: Potential carbon emissions dominated by carbon dioxide from thawed permafrost soils, Nature Climate Change, 6, 950–953,
https://doi.org/10.1038/nclimate3054, 2016.

Slater, A. G. and Lawrence, D. M.: Diagnosing Present and Future Permafrost from Climate Models, Journal of Climate, 26, 5608–5623,
https://doi.org/10.1175/JCLI-D-12-00341.1, 2013.

660   Teufel, B. and Sushama, L.: Abrupt changes across the Arctic permafrost region endanger northern development, Nature Climate Change, 9,
858–862, https://doi.org/10.1038/s41558-019-0614-6, 2019.

Turetsky, M. R., Abbott, B. W., Jones, M. C., Walter Anthony, K., Olefeldt, D., Schuur, E. A. G., Koven, C., McGuire, A. D., Grosse, G.,
Kuhry, P., Hugelius, G., Lawrence, D. M., Gibson, C., and Sannel, A. B. K.: Permafrost collapse is accelerating carbon release, Nature,
569, 32–34, https://doi.org/10.1038/d41586-019-01313-4, 2019.

665   Turetsky, M. R., Abbott, B. W., Jones, M. C., Anthony, K. W., Olefeldt, D., Schuur, E. A. G., Grosse, G., Kuhry, P., Hugelius, G., Koven, C.,
Lawrence, D. M., Gibson, C., Sannel, A. B. K., and McGuire, A. D.: Carbon release through abrupt permafrost thaw, Nature Geoscience,
13, 138–143, https://doi.org/10.1038/s41561-019-0526-0, 2020.

Vincent, W. F., Lemay, M., and Allard, M.: Arctic permafrost landscapes in transition: towards an integrated Earth system approach, Arctic
Science, 3, 39–64, https://doi.org/10.1139/as-2016-0027, 2017.

670   Wagner, A. M., Lindsey, N. J., Dou, S., Gelvin, A., Saari, S., Williams, C., Ekblaw, I., Ulrich, C., Borglin, S., Morales, A., and Ajo-
Franklin, J.: Permafrost Degradation and Subsidence Observations during a Controlled Warming Experiment, Scientific Reports, 8, 1–9,
https://doi.org/10.1038/s41598-018-29292-y, 2018.

Walter Anthony, K., Deimling, T. S. v., Nitze, I., Frolking, S., Emond, A., Daanen, R., Anthony, P., Lindgren, P., Jones, B., and Grosse,
G.: 21st-century modeled permafrost carbon emissions accelerated by abrupt thaw beneath lakes, Nature Communications, 9, 3262,
675   https://doi.org/10.1038/s41467-018-05738-9, 2018.

Westermann, S., Langer, M., Boike, J., Heikenfeld, M., Peter, M., Etzelmüller, B., and Krinner, G.: Simulating the thermal regime and thaw processes of ice-rich permafrost ground with the land-surface model CryoGrid 3, Geosci. Model Dev., 9, 523–546, https://doi.org/10.5194/gmd-9-523-2016, 2016.

Zhang, W., Witharana, C., Liljedahl, A., Kanevskiy, M., Zhang, W., Witharana, C., Liljedahl, A. K., and Kanevskiy, M.: Deep Convolutional

680   Neural Networks for Automated Characterization of Arctic Ice-Wedge Polygons in Very High Spatial Resolution Aerial Imagery, Remote Sensing, 10, 1487, https://doi.org/10.3390/rs10091487, 2018.

Zhang, W., Liljedahl, A. K., Kanevskiy, M., Epstein, H. E., Jones, B. M., Jorgenson, M. T., and Kent, K.: Transferability of the Deep Learning Mask R-CNN Model for Automated Mapping of Ice-Wedge Polygons in High-Resolution Satellite and UAV Images, Remote Sensing, 12, 1085, https://doi.org/10.3390/rs12071085, 2020.

685   Zuecco, G., Rinderer, M., Penna, D., Borga, M., and van Meerveld, H. J.: Quantification of subsurface hydrologic connectivity in four headwater catchments using graph theory, Science of The Total Environment, 646, 1265–1280, https://doi.org/10.1016/j.scitotenv.2018.07.269, 2019.

Zweigel, R., Westermann, S., Nitzbon, J., Langer, M., Boike, J., Etzelmüller, B., and Vikhamar Schuler, T.: Simulating snow redistribution and its effect on the ground thermal regime at a high-Arctic site on Svalbard, Journal of Geophysical Research: Earth Surface, in review,

690   2020.